# Metamaterial-based Luneburg Lens for RF Applications Using Additive Manufacturing

Emma M. Sadoyan, Mark S. Mnatsakanyan, and Suren G. Eyramjyan

*ATG CJSC, Yerevan, Armenia*

https://doi.org/10.26636/jtit.2024.4.1786

**Abstract — This article takes a detailed look at modeling, simulating, calculating, and fabricating a Luneburg lens using a single material and advanced 3D printing technology. The Luneburg lens is a type of gradient index lens that is spherically symmetrical, which simplifyies its manufacturing process and enhances its structural stability. However, fabrication may be expensive due to the special materials required for manufacturing. Discovering simpler and cost-effective production methods would enable the wider use of Luneburg lenses across various fields. The objective of this study was to use the lens to increase the gain and directivity of antennas at 5.8 GHz while maintaining a compact lens size and using low-cost material, such as ABS-like filament. A single-cell cross-shaped structure was utilized to construct the lens using 3D printing technology.**

***Keywords — 3D printing, ABS plastic, Luneburg lens, metamaterial***

## 1. Introduction

The Luneburg lens [1] is a type of gradient index lens (GRIN) characterized by the fact that its refractive index $n$ varies gradually from the center outward. The gradual change in the refractive index causes a curved path for the radiation beam [2].

Ideally, the refractive index of the inner layer of the Luneburg lens should be $\sqrt{2}$ and ought to gradually decrease towards the outer layer, until it reaches a value of 1, with the variation complying with the following formula:

$$n(r) = \sqrt{\varepsilon(r)} = \sqrt{2 - \left(\frac{r}{R}\right)^2}, \tag{1}$$

where $\varepsilon$ is the effective dielectric permittivity, $r$ is the radius of each layer, and $R$ is the radius of the outer layer [1]–[4]. The Luneburg lens finds various applications, including in acoustics [5]–[8], optics [9]–[12], as well as antenna, communication and radar system designs [13]–[17].

This paper presents a detailed study of the process of designing a Luneburg lens. It analyzes the use of various structures to boost the performance at 5.8 GHz, as well as to increase gain and directivity of antennas in RF and communication systems. This article focuses on using ABS-like filament as a cost-effective material and a cross-shaped structure to simplify the manufacturing process with the use of advanced 3D printing technology.

The goal is to demonstrate how this method is capable of increasing antenna gain and directivity while maintaining a compact lens size.

## 2. Method

The 5.8 GHz frequency band was selected for this study because it falls within the unlicensed part of the spectrum and is widely used in wireless applications, making it a practical choice for antenna system development. This frequency band also offers the advantage of a shorter wavelength, approximately 5.17 cm, allowing for a more compact lens design. The wavelength is a crucial parameter in determining the physical dimensions of the Luneburg lens, as its geometry must be proportional to the operating wavelength to ensure effective propagation and focusing.

In alignment with the design approach used by Fortify (in collaboration with Rogers Corporation) [18], [19], a 6-layer configuration was adopted for the Luneburg lens, with the radius values of each layer corresponding to those in their model. Although the chosen lens diameter was 6 cm, slightly larger than the desired wavelength of 5.17 cm, this increase in size provides a greater surface area for wave propagation, contributing to improved gain and directivity.

The multilayer design enables the required refractive index gradient to be achieved, which is essential for accurate wave focusing and efficient propagation. Figure 1 illustrates the

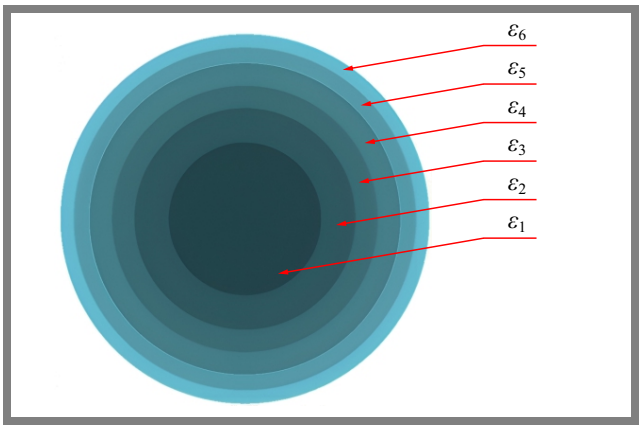


**Fig. 1.** Luneburg lens layers.

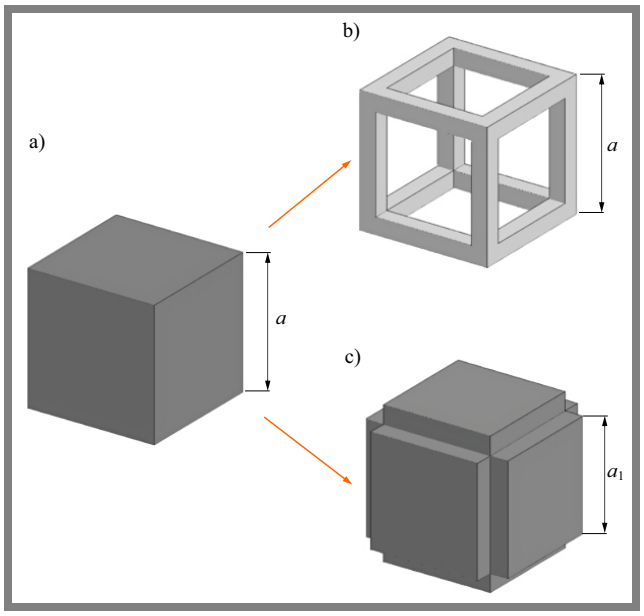


**Fig. 2.** A cube with $a$ side a), the air part of the cube b), and the solid part of the cube (the unit cell of the lens) c).

layer numbering and the corresponding dielectric permittivities $\varepsilon_1, \varepsilon_2, \ldots, \varepsilon_6$. The permittivity values for each layer were determined through a series of simulations of the lens aimed at identifying appropriate values to achieve gain and directivity at 5.8 GHz. Detailed information on the simulation methodology is provided in Section 4.

To achieve homogeneity in each layer of the lens, a cubic structure, as shown in Fig. 2a, was divided into two parts, with the air part being subtracted to create a cross-shaped single-cell design illustrated in Fig. 2b. This approach allows for a proportional arrangement of unit cells, which is essential to achieve the desired refractive index gradient. Relative permittivity values were adjusted keeping the length of side $a$ constant and varying the length of side $a_1$ for each layer. A similar method was used for the Luneburg acoustic lens in [7].

## 3. Lens Design

To determine the value of side $a_1$ for each layer, it was necessary to establish the relationship between side $a_1$ (Fig. 2) and the relative permittivity values of each layer. To achieve this, the rule of mixtures [20], [21] was applied. Therefore, the effective permittivity is calculated as follows:

$$\varepsilon_{eff} = \varepsilon_a f_a + \varepsilon_h f_h, \tag{2}$$

where $\varepsilon_a$ and $f_a$ are the relative permittivity and the air fill fraction, respectively, while $\varepsilon_h$ and $f_h$ are the relative permittivity and the fill fraction of the host material. The relative permittivity of air is $\varepsilon_a = 1$, while the relative permittivity of the host material, represented as $\varepsilon_h$, is that of ABS plastic. Studies referenced in [22]–[25] indicate that the relative dielectric constant of ABS plastic varies between 2.2 and 3.1. Therefore, an average dielectric permittivity value of $\varepsilon_h = 2.75$ and a tangent loss of 0.012 were selected for the calculations.

**Tab. 1.** Parameters of the Luneburg lens for each layer.

| Layer | 1 | 2 | 3 | 4 | 5 | 6 |
|---|---|---|---|---|---|---|
| Radius [mm] | 12.4 | 18 | 21.7 | 25.4 | 27.9 | 30 |
| $a_1$ [mm] | 1.09 | 0.97 | 0.94 | 0.73 | 0.58 | 0.26 |
| $\varepsilon_{eff}$ | 1.92 | 1.77 | 1.74 | 1.49 | 1.33 | 1.07 |

The filling fraction of the air is:

$$f_a = \frac{Number\ of\ holes \times Volume\ of\ a\ single\ hole}{Total\ volume}, \tag{3}$$

and the filling fraction of the host material is:

$$f_h = \frac{Total\ vol. - No.\ of\ holes \times Vol.\ of\ a\ single\ hole}{Total\ volume}, \tag{4}$$

The number of holes in this work is denoted with $N_{hole}$, the volume of a single hole with $V_{hole}$, and the total volume of each layer with $V_{total}$. The volume of the cube shown in Fig. 2a was also needed in the calculations, denoted by $V_{cube}$. By substituting the defined variables into Eqs. (3) and (4), the following form is derived:

$$f_a = \frac{N_{hole} \times V_{hole}}{V_{Total}}, \tag{5}$$

$$f_h = 1 - \frac{N_{hole} \times V_{hole}}{V_{Total}}. \tag{6}$$

As previously discussed, each of the cubes consists of two parts: an air hole part and a solid or the unit cell part (Fig. 2). To quantify the volume of holes within the sphere, the total volume of each layer was divided by the volume of a cube, allowing one to determine how many of these cubic structures could fit within the spherical volume and subsequently calculate the number of holes:

$$N_{hole} = \frac{V_{total}}{V_{cube}}. \tag{7}$$

The volume of the hole is:

$$V_{hole} = V_{cube} - V_{unit\_cell}. \tag{8}$$

The volume of the cube is $V_{cube} = a^3$ and the volume of the unit cell is equal to the volume of the cross-shaped structure shown in Fig. 2c:

$$V_{unit\_cell} = 2\,a_1^3 + 3\,a_1^2\,a \tag{9}$$

From Eqs. (8) and (9):

$$V_{hole} = a^3 - (2\,a_1^3 + 3\,a_1^2\,a). \tag{10}$$

After inserting the appropriate variables and constants into Eq. (2) and applying mathematical transformations, the relationship between side $a_1$ and the effective dielectric permittivity is derived as follows:

$$2\,a_1^3 - 3\,a_1^2\,a + a^3 = V_{cube}\,\frac{\varepsilon_{eff} - \varepsilon_h}{1 - \varepsilon_h}, \tag{11}$$

where $a$ and $\varepsilon_h$ are constants mentioned earlier, the side size $a$ was set to 2.1 mm, matching the thickness of the thinnest layer (6th layer). Upon solving Eq. (11), the results presented in Tab. 1 were obtained.

## 4. Simulation

To evaluate the impact of the approach adopted before performing any manufacturing operations, simulations were conducted using Altair Feko electromagnetic simulator software. First, a baseline radiation pattern was established by simulating a standalone rectangular patch antenna shown in Fig. 3. Next, the lens was positioned in front of the antenna, and the simulation was repeated to assess the lens' influence on the radiation pattern of the patch antenna. Subsequently, the lens was modeled as a continuous structure, consisting of six layers with the corresponding thicknesses, as illustrated in Fig. 1. Each layer was assigned the appropriate dielectric properties, and the final structure with a patch antenna is shown in Fig. 3.

The Luneburg lens was placed 20 mm away from the patch antenna and the resulting radiation pattern, with the lens, was obtained. A comparison between the radiation pattern of the patch antenna solo and that of the antenna with the lens is presented in Fig. 4. The red line represents the far-field radiation of the antenna without the lens, while the blue line shows the radiation pattern after the lens was introduced.

The simulation results showed that antenna performance was significantly improved after the Luneburg lens was introduced. The antenna gain increased by approximately 4.6 dBi, reaching a final value of 8.8 dBi. This increase in gain was due to the lens' ability to focus and concentrate the radiated energy, resulting in a more directional beam. Additionally, the half-power beamwidth (HPBW) was reduced from 92° to approximately 45°. This narrower beamwidth indicates more focused radiation, which can be beneficial in applications requiring precise energy transfer or better directivity.

The simulation was carried out with a continuous structure shown in Fig. 3. To avoid an excessive number of meshes and to shorten the overall simulation and design time, a portion of each layer of the lens was simulated using the proposed structure, rather than simulating the entire lens, to ensure that the desired dielectric properties, particularly dielectric permittivity (Tab. 1), were achieved for each layer. The results closely matched the target values obtained from the continuous lens simulation.

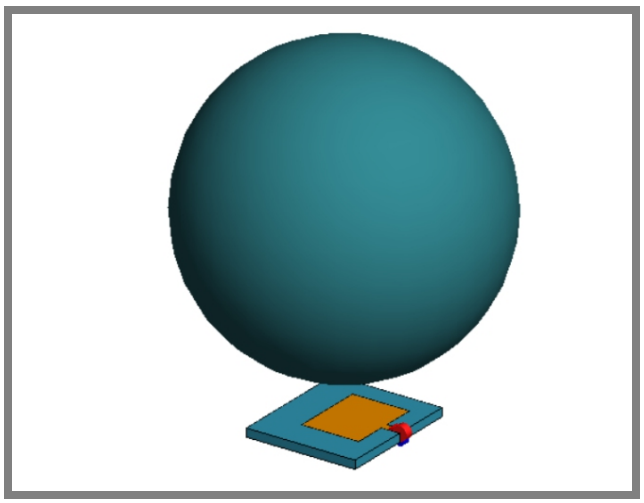

**Fig. 3.** The lens with the patch antenna.

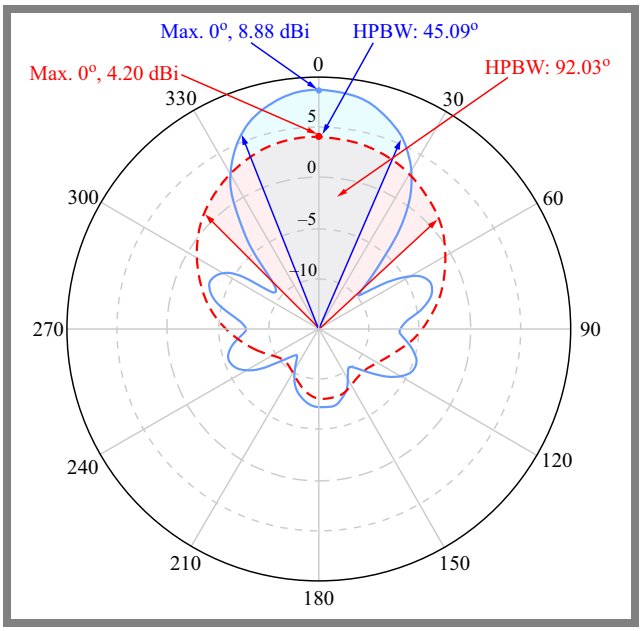


**Fig. 4.** Comparison between the far fields of the patch antenna only (red line) and the patch antenna with the lens at 5.8 GHz (blue line).

## 5. Design

Based on the data presented in Tab. 1, the lens was designed using SolidWorks software, with the final model shown in Fig. 5.

Stereolithography (SLA), a high-accuracy 3D printing technique, was used for fabrication. Although the calculations presented in Section 3 were based on parameters for ABS plastic, the lens was constructed using an ABS-like filament, exhibiting similar material properties, due to the requirements of the 3D printing method used. Figure 6 shows the printed lens and provides a closer view of its structure, highlighting the cross-shaped cells within.

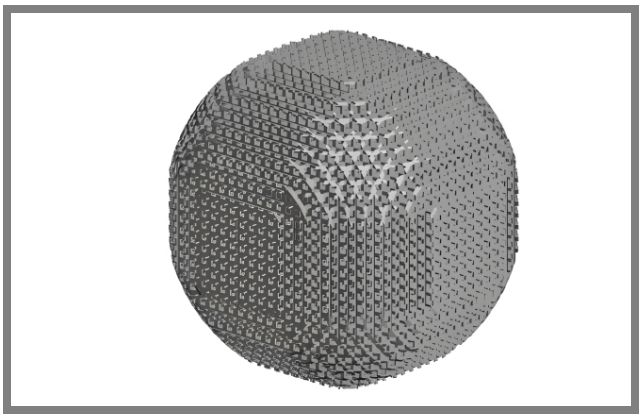

**Fig. 5.** The 3D model of the lens.

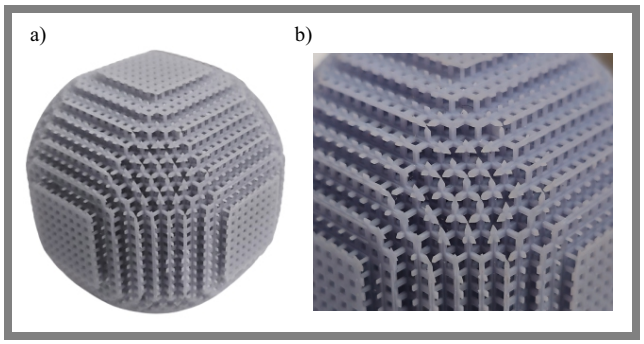


**Fig. 6.** Printed lens a) and a closer look at its structure b).

## 6. Testing Results

In the course of the measurements, the receiving and transmitting antennas were placed 28.2 cm apart, with the Luneburg lens positioned 2 cm from the transmitting antenna. The measurement system was enclosed, on all sides, within an anechoic chamber to minimize external interference and ensure accuracy of the data collection process. The results are depicted in Fig. 7, showing a gain improvement of approximately 4.2 dB and a narrowing of the half-power beamwidth (HPBW). These results indicate the focusing effect of the Luneburg lens, which is consistent with expectations based on the simulation data.

Referring to Fig. 4, it is evident that the real measurement results and the simulated ones exhibit a similar overall pattern. In both cases, the addition of the lens has led to an increase in gain and a reduction in HPBW. The simulated results showed a gain increase of approximately 4.6 dB, while the real-world measurements indicated a gain improvement of 4.2 dB. This slight difference may result from fabrication tolerances, material imperfections, or slight misalignments during testing.

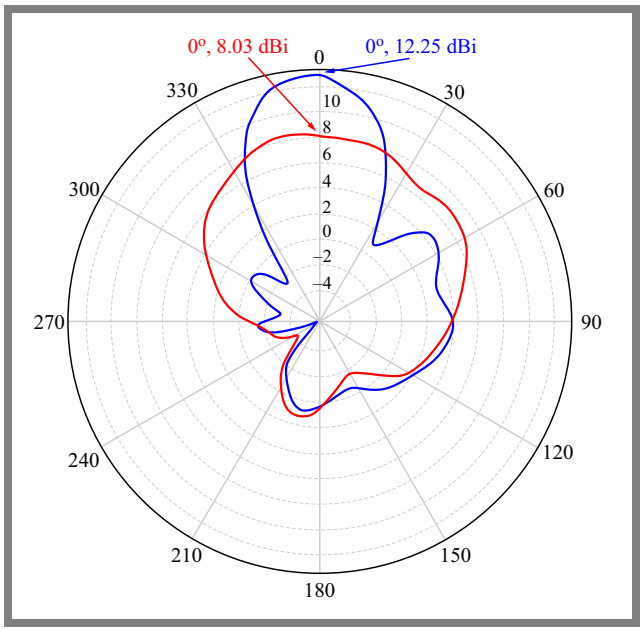


**Fig. 7.** Radiation patterns of the measured patch antenna (red line) and the patch antenna with the lens (blue line).

Both the simulated and measured results indicated a reduction of approximately two times in HPBW, with slight differences. This reduction demonstrates the effectiveness in focusing the beam. Differences in exact values could be attributed to real-world factors, such as environmental conditions, inaccuracies in the printed lens structure or differences in material properties between the simulated ABS filament and the actual ABS-like filament used in during the fabrication process.

## 7. Conclusion

This work demonstrated the effectiveness of using the rule of mixtures to determine the appropriate material-air ratio for the lens structure. This method enabled the fabrication of a gradient index (GRIN) Luneburg lens with suitable dielectric properties, achieved without relying on more complex, time-consuming, or costly processes. The results showed a gain improvement of approximately 4.2 dB and a significant narrowing of the half-power beamwidth (HPBW), confirming the enhanced performance of the antenna when the lens was integrated therewith. The successful use of 3D printing for lens construction further highlights the potential of additive manufacturing techniques in producing customized metamaterials.

## References

[1] R.K. Luneburg, *Mathematical Theory of Optics*, University of California Press, 448 p., 1964 (https://doi.org/10.1525/9780520328266).

[2] J.E. Gómez-Correa *et al.*, "Generalization of Ray Tracing in Symmetric Gradient-index Media by Fermat's Ray Invariants", *Optics Express*, vol. 29, no. 21, pp. 33009–33026, 2021 (https://doi.org/10.1364/OE.440410).

[3] N. Korotkov and Y.E. Mitelman, "Simulation of Spherical Luneburg Lens Using Numerical Electrodynamic Methods", *Proceedings of Information Technologies, Telecommunications and Control Systems*, 2017 (https://ceur-ws.org/Vol-2035/paper13.pdf).

[4] Q. Cheng, M. Naeem, and Y. Hao, "Composite Luneburg Lens Based on Dielectric or Plasmonic Scatterers", *Optics Express*, vol. 27, no. 8, pp. 10946-10960, 2019 (https://doi.org/10.1364/OE.27.010946).

[5] Y. Xie *et al.*, "Acoustic Imaging with Metamaterial Luneburg Lenses", *Scientific Reports*, vol. 8, art. no. 16188, 2018 (https://doi.org/10.1038/s41598-018-34581-7).

[6] L. Zhao, T. Horiuchi, and M. Yu, "Directional Acoustic Luneburg Lens Waveguide", *ArXiv*, 2022 (https://doi.org/10.48550/arXiv.2201.01876).

[7] L. Zhao, T. Horiuchi, and M. Yu, "Broadband Acoustic Collimation and Focusing Using Reduced Aberration Acoustic Luneburg Lens", *Journal of Applied Physics*, vol. 130, no. 21, art. no. 214901, 2021 (https://doi.org/10.1063/5.0064571).

[8] L. Zhao *et al.*, "A Review of Acoustic Luneburg Lens: Physics and Applications", *Mechanical Systems and Signal Processing*, vol. 199, art. no. 110468, 2023 (https://doi.org/10.1016/j.ymssp.2023.110468).

[9] A. Di Falco, S.C. Kehr, and U. Leonhardt, "Luneburg Lens in Silicon Photonics", *Optics Express*, vol. 19, no. 6, pp. 5156–5162, 2011 (https://doi.org/10.1364/OE.19.005156).

[10] C.E. Garcia-Ortiz *et al.*, "Plasmonic Metasurface Luneburg Lens", *Photonics Research*, vol. 7, no. 10, pp. 1112–1118, 2019 (https://doi.org/10.1364/PRJ.7.001112).

[11] T. Driscoll *et al.*, "Performance of a Three Dimensional Transformation-optical-flattened Luneburg Lens", *Optics Express*, vol. 20, no. 12, pp. 13262–13273, 2012 (https://doi.org/10.1364/OE.20.013262).

[12] W. Dong, Y. Lai, and Jin Hu, "Detecting Spatial Chirp Signals by Luneburg Lens Based Transformation Medium", *Optics Express*, vol. 30, no. 6, pp. 9773–9789, 2022 (https://doi.org/10.1364/OE.453937).

[13] A. Demetriadou and Y. Hao, "Slim Luneburg Lens for Antenna Applications", *Optics Express*, vol. 19, no. 21, pp. 19925–19934, 2011 (https://doi.org/10.1364/OE.19.019925).

[14] H. Saghlatoon, M.M. Honari, S. Aslanzadeh, and R. Mirzavand, "Electrically-small Luneburg Lens for Antenna Gain Enhancement Using New 3D Printing Filling Technique", *AEU - International Journal of Electronics and Communications*, vol. 124, art. no. 153352, 2020 (https://doi.org/10.1016/j.aeue.2020.153352).

[15] Tech-Lightenment, "The Future Satellite Antenna-Luneburg Lens Antenna", (https://tech-lightenment.blogspot.com).

[16] H.-T. Chou *et al.*, "Optimization of Three-Dimensional Multi-Shell Dielectric Lens Antennas to Radiate Multiple Shaped Beams for Cellular Radio Coverage", *IEEE Access*, vol. 7, pp. 182974–182982, 2019 (https://doi.org/10.1109/ACCESS.2019.2959277).

[17] B. Ahn *et al.*, "Wide-angle Scanning Phased Array Antenna Using High Gain Pattern Reconfigurable Antenna Elements", *Scientific Reports*, vol. 9, art. no. 18391, 2019 (https://doi.org/10.1038/s41598-019-54120-2).

[18] Fortify, "Low Loss Dielectric 3D Printing", (https://3dfortify.com/wp-content/uploads/2022/01/RF-One-Pager_RevF.pdf).

[19] Fortify, "3D Printed Dielectric Lenses Increase Antenna Gain and Widen Beam Scanning Angle", (https://3dfortify.com/wp-content/uploads/2021/07/Fortify_3D-Printed-Dielectric-Lenses-White-Paper_RevB.pdf).

[20] University of Cambridge, "Derivation of the Rule of Mixtures and Inverse Rule of Mixtures", (https://www.doitpoms.ac.uk/tlplib/bones/derivation_mixture_rules.php).

[21] University of Cambridge, "Stiffness of Long Fibre Composites", (https://www.doitpoms.ac.uk/tlplib/fibre_composites/stiffness.php).

[22] A. Al Takach *et al.*, "Two-line Technique for Dielectric Material Characterization with Application in 3D-printing Filament Electrical Parameters Extraction", *Progress In Electromagnetics Research M*, vol. 85, pp. 195–207, 2019 (https://doi.org/10.2528/PIERM19071702).

[23] N. Reyns *et al.*, "Complex Dielectric Permittivity of Engineering and 3D-printing Polymers at Q-band", *Journal of Infrared, Millimeter, and Terahertz Waves*, vol. 39, no. 11, pp. 1140–1147, 2018 (https://doi.org/10.1007/s10762-018-0528-9).

[24] B. Behzadnezhad, B.D. Collick, N. Behdad, and A.B. McMillan, "Dielectric Properties of 3D-printed Materials for Anatomy Specific 3D-printed MRI Coils", *Journal of Magnetic Resonance*, vol. 289, pp. 113–121, 2018 (https://doi.org/10.1016/j.jmr.2018.02.013).

[25] T. Hayat, M.U. Afzal, A. Lalbakhsh, and K.P. Esselle, "Additively Manufactured Perforated Superstrate to Improve Directive Radiation Characteristics of Electromagnetic Source", *IEEE Access*, vol. 7, pp. 153445–153452, 2019 (https://doi.org/10.1109/ACCESS.2019.2948735).

**Emma M. Sadoyan**
https://orcid.org/0009-0006-7824-7507
E-mail: emma.sadoyan@advanced.am
ATG CJSC, Yerevan, Armenia
https://advanced.am

**Mark S. Mnatsakanyan**
https://orcid.org/0009-0000-9403-6415
E-mail: mark.mnatsakanyan@advanced.am
ATG CJSC, Yerevan, Armenia
https://advanced.am

**Suren G. Eyramjyan**
https://orcid.org/0009-0001-2694-5059
E-mail: suren.eyramjyan@advanced.am
ATG CJSC, Yerevan, Armenia
https://advanced.am